Tailoring intermediate switching states in magnetic $La_{0.67}Sr_{0.33}MnO_3$ multilayers

Song Dai,[1,*] Grace L. Causer,[2,*] Chengcheng Xu,[1] Mengsha Li,[3] Kun Han,[1] Liqiang Xu,[1] Zhipeng Xu,[4] Bixing Yan,[3] Guanyin Gao,[5] Gan Moog Chow,[3] Wenbin Wu,[5] Pingfan Chen,[1,†] and Zhen Huang[1,4,‡]

[1]*Information Materials and Intelligent Sensing Laboratory of Anhui Province, Institutes of Physical Science and Information Technology, Anhui University, Hefei 230601, People's Republic of China*

[2]*Physics Department, Technical University of Munich, 85748 Garching, Germany*

[3]*Department of Materials Science and Engineering, National University of Singapore, 117575 Singapore*

[4]*Stony Brook Institute at Anhui University, Anhui University, Hefei 230039, People's Republic of China*

[5]*Hefei National Laboratory for Physical Sciences at Microscale, University of Science and Technology of China, Hefei 230026, People's Republic of China*

(Received 20 August 2023; revised 18 July 2024; accepted 23 July 2024; published 8 August 2024)

Intermediate switching states are of great interest for developing advanced magnetic memories. In this paper, the magnetic switching process is studied in the multilayers that are fabricated using two distinct $La_{0.67}Sr_{0.33}MnO_3$ building blocks, i.e., $PbTiO_3/La_{0.67}Sr_{0.33}MnO_3/NdGaO_3$ (block A) and $PbTiO_3/La_{0.67}Sr_{0.33}MnO_3/PbTiO_3$ (block B) with different intralayer ferromagnetic couplings. Accordingly, the multilayer that consists of two types of $La_{0.67}Sr_{0.33}MnO_3$ blocks is featured by two distinct Curie temperatures and coercive fields, as expected. On the other hand, the sample only composed of block B displays a single Curie temperature but two unexpected coercive fields. While the single Curie temperature indicates the same intralayer ferromagnetic coupling in all $La_{0.67}Sr_{0.33}MnO_3$ sublayers, two coercive fields suggest the existence of an intermediate switching state. The detailed study on polarized neutron reflectometry reveals that this intermediate state exhibits a gradual change of magnetization, from parallel to antiparallel with respect to the external magnetic field, across $La_{0.67}Sr_{0.33}MnO_3$ sublayers approaching the substrate. The competition between the interlayer exchange and magnetostatic interaction is highlighted to show the intermediate magnetization structure of $La_{0.67}Sr_{0.33}MnO_3$ multilayers with identical intralayer coupling. Our findings shed light on controlling switching states and may contribute to the design of nanoscale high-density magnetic memories.

DOI: 10.1103/PhysRevB.110.054417

I. INTRODUCTION

The precise manipulation of magnetization switching provides valuable insights into the complex interplay of spins, holding significant potential to build topological spin texture with emergent physics properties [1–4] and develop high-efficiency magnetic devices [5–8]. Especially, the interplay between the intralayer coupling and interlayer exchange greatly enriches magnetization structures of multilayers, offering additional tunability for key magnetic parameters such as Curie temperature (T_C) and coercive field (H_c) that are essential for practical applications [9–12]. Synthetic antiferromagnets, for instance, where neighboring magnetic sublayers exhibit antiparallel alignment of magnetizations, show promise in reducing stray fields, thereby improving data storage density and reliability in magnetic devices [13,14].

However, achieving the effective control on individual magnetic sublayers within a multilayer is not straightforward. One feasible approach is to use various magnetic materials with different coercivities to form magnetic sublayers, which result in multiple coercivities during the magnetization process. In this case, extra attention needs to be paid to solve the possible incompatibility stemming from distinct lattice structures, growth parameters, and working conditions of these selected magnetic materials. An alternative approach is to design the multilayer using only one specific magnetic material, of which the magnetic coercivity is subject to the interfacial boundaries, thus allowing for the tunability within each sublayer. Pursuing the second approach requires a sophisticated understanding and utilization on the interface engineering. The ferromagnetic $La_{0.67}Sr_{0.33}MnO_3$ (LSMO) may be a good candidate for the second approach [15,16]. Recent studies have documented that a wide tunable range of magnetic parameters was achieved in the interface-engineered LSMO heterostructures [17–19]. It is understood that an adjacent layer can modify the oxygen octahedral rotation [17] and charge concentration [18,19], via oxygen octahedral coupling and interfacial charge transfer respectively, to alter the intralayer magnetic coupling of LSMO sublayers. With this rationale, it is reasonable to hypothesize that a multilayer sample containing several types of LSMO-based building blocks will be featured by several field-separated coercivities and intermediate switching states, due to different intralayer couplings within magnetic sublayers. Meanwhile, for a multilayer only consisting of one type of LSMO blocks with identical

*These authors contributed equally to this work.
†Contact author: chenpf@ahu.edu.cn
‡Contact author: huangz@ahu.edu.cn

intralayer coupling, one would intuitively predict a collective switching of all LSMO blocks with a single coercivity in the hysteresis loop.

In this paper, two distinct LSMO building blocks, namely $PbTiO_3$/LSMO/$NdGaO_3$ as block A and $PbTiO_3$/LSMO/$PbTiO_3$ as block B, are used to construct LSMO-based multilayers. The nonmagnetic $PbTiO_3$ spacer and $NdGaO_3$ substrate are applied to control the intralayer coupling of LSMO sublayers via interfacial charge transfer and oxygen octahedral coupling. The multilayer sample A1B7 is designed to contain one block A and seven blocks B, demonstrating two corresponding Curie temperatures and magnetic coercivities. However, sample B8 consisting of eight blocks B with identical intralayer coupling shows one Curie temperature, accompanied by two unexpected field-separated coercivities. This observation cannot be ascribed to the interface engineering regarding oxygen octahedral coupling and interfacial charge transfer. Instead, we discuss the interplay between ferromagnetic interlayer exchange and magnetostatic interaction to account for the intermediate switching state with antiparallelly magnetized sublayers in LSMO/$PbTiO_3$ multilayers.

II. EXPERIMENT

A. Sample preparation

Pulsed laser deposition. LSMO multilayers were fabricated on (110)-orientated $NdGaO_3$ substrates by pulsed laser deposition (PLD) with *in situ* reflection high-energy electron diffraction (RHEED). For all studied multilayers, the thickness of the LSMO sublayer was fixed at 9 unit cells, while the thickness of $PbTiO_3$ sublayers was kept at 12 unit cells. During the deposition, the growth temperature was kept at 750 °C, oxygen partial pressure at 100 mTorr, and the laser energy at 1.8 J/cm^2. After the deposition, the *in situ* annealing was performed at 600 °C in 1 atm oxygen for 15 min.

B. Magnetic and transport property measurements

Superconducting quantum interference device vibrating sample magnetometer. The volume-averaged magnetic properties were measured using a superconducting quantum interference device vibrating sample magnetometer (SQUID VSM, Quantum Design). The temperature-dependent magnetic moment was measured upon warming in 200 Oe, following the field cooling from 300 to 10 K in 2000 Oe. For the field-dependent magnetic moment, the sample was first zero-field cooled to the target temperature, and then measured by sweeping the magnetic field.

Polarized neutron reflectometry. Polarized neutron reflectometry (PNR) measurements were conducted on the Platypus time-of-flight reflectometer located at the Australian Nuclear Science and Technology Organisation (ANSTO) [20,21]. Data were obtained with full polarization analysis as a function of the scattering vector $Q = 4\pi \sin(\theta)/\lambda$, where λ represents the neutron wavelength and θ is the scattering angle. Non-spin-flip (NSF) reflectivities, i.e., $R++$ and $R--$, probe the sample's nuclear structure and the component of the magnetization parallel to the neutron polarization axis, while spin-flip (SF) reflectivities, i.e., $R+-$ and $R-+$, probe the component of the sample's magnetic moment perpendicular to the neutron polarization axis only. Taken together the four reflectivities ($R++$, $R--$, $R+-$, and $R-+$) allow the in-plane components of the sample's magnetization parallel and perpendicular to the neutron polarization axis to be spatially resolved to provide a quantitative measurement of the sample's magnetic moment per unit volume as a function of sample depth. Specifically, the normalized difference between the $R++$ and $R--$ reflectivity as a function of Q is directly proportional to the in-plane magnetic spin configuration of the sample. Furthermore, the symmetrical arrangement of the electromagnet and the pre- and postsample guide field coils of the Platypus instrument [21] allows both positive and negative fields to be applied to the sample space without depolarizing the neutron beam. In our cases, the sample was initially field cooled from room temperature under a magnetic field of 5000 Oe, applied parallelly to the [1–10] axis (indicated as +5000 Oe). Subsequent $R++$, $R--$, $R-+$, and $R+-$ data were recorded at 10 K at target intermediate magnetic fields along the [−110] axis (indicated as −110 Oe for sample A1B7 and −260 Oe for sample B8) during magnetic reversal. For all fields, the SF intensity is several orders of magnitude smaller than the NSF one (as shown in Supplemental Material Fig. S1 [22]), indicating a neglectable magnetization in the plane of the film perpendicular to the external magnetic field during magnetic reversal. PNR data analysis was performed using the SIMULREFLEC software package [23].

Physical properties measurement system. The transport measurements were performed using the van der Pauw method with the physical properties measurement system (PPMS, Quantum Design).

C. Sample characterizations

High-resolution x-ray reflectometry. The periodic chemical structures of the samples were characterized by high resolution x-ray reflectometry (HR-XRR, Panalytical, X'pert) utilizing Cu $K_{\alpha 1}$ radiation ($\lambda = 1.5406$ Å).

Atomic force microscopy. The surface of the samples was examined by atomic force microscopy (AFM, Cypher S, Oxford Instrument) with TESPA-V2 tips.

Scanning transmission electron microscopy. The sample for scanning transmission electron microscopy (STEM) analysis was prepared by focused ion beam (FIB) with 30-kV Ga ions, followed by a 2-kV low voltage cleaning step. High-resolution STEM-annular dark-field (ADF) imaging was conducted using the JEOL-ARM200F microscope equipped with an ASCOR aberration corrector and a cold-field emission gun, operating at 200 kV. The high-angle annular dark-field (HAADF) images were acquired using a probe-forming aperture of 30 mrad and a collection angle ranging 68–280 mrad.

III. RESULTS AND DISCUSSION

A. Designs of LSMO heterointerfaces

Figure 1 compares two LSMO-based building blocks that are used in our multilayer samples, i.e., block A of $PbTiO_3$/LSMO/$NdGaO_3$ [Fig. 1(a)] and block B of $PbTiO_3$/LSMO/$PbTiO_3$ [Fig. 1(b)] (also see Fig. S2 in the

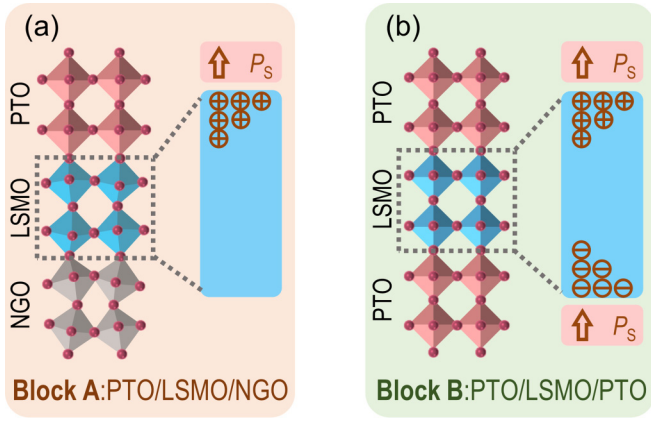

FIG. 1. (a) Block A of $PbTiO_3$/LSMO/$NdGaO_3$ and (b) block B of $PbTiO_3$/LSMO/$PbTiO_3$ mediated by the oxygen octahedral coupling and interfacial charge modulation. Here, $NdGaO_3$ ($PbTiO_3$) possesses an orthorhombic (tetragonal) crystal structure with a rotation pattern $c^+a^-a^-$ ($a^0a^0a^0$), resulting in the more intensive octahedral rotation in block A. The assumed *upward* spontaneous polarization P_S can affect the charge concentration and distribution in the adjacent LSMO, leaving the increased (unchanged) average hole concentration in block A (B), respectively.

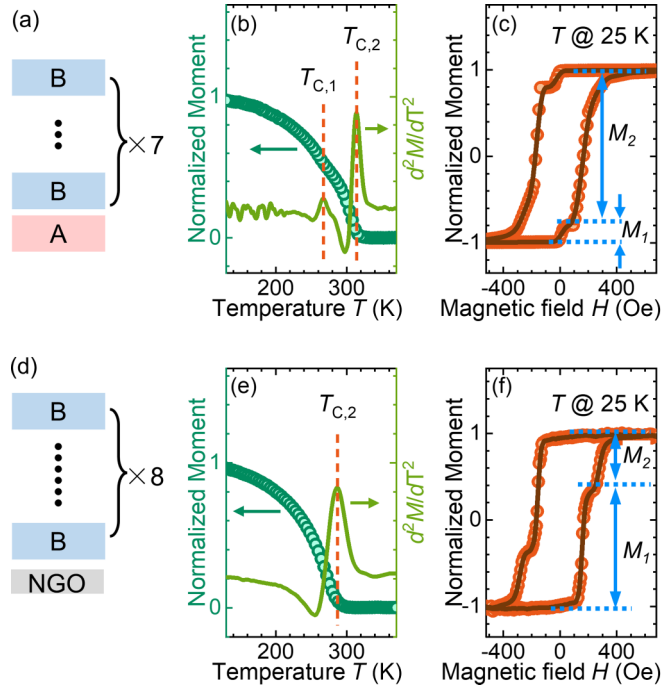

FIG. 2. The structural sketches, $M(T)$ and $M(H)$ curves are shown for sample A1B7 in (a)–(c) and sample B8 in (d)–(f), respectively. In (a) and (d), the schematics of multilayer samples A1B7 and B8 are demonstrated. In (b), (c), (e), and (f), magnetization data [i.e., $M(T)$ curves and $M(H)$ curves at 25 K] are collected, where $T_{C,1}$ and $T_{C,2}$ are determined by the peak positions of d^2M/dT^2 curves and indexed by the red dashed lines. In (c) and (f), M_1 and M_2 represent the switched and unswitched magnetic moments for the intermediate switching state with a magnetic field between $H_{c,1}$ and $H_{c,2}$.

Supplemental Material [22]). First, these materials share similar bulk lattice parameters. When indexed by a pseudocubic ABO_3 lattice, the close in-plane lattice constants (i.e., 3.873 Å for LSMO, 3.867 Å for $NdGaO_3$, and 3.902 Å for $PbTiO_3$) [24–26] lead to the high-quality coherent growth in both blocks A and B (also see Fig. S3 in the Supplemental Material [22]). Second, if considering different oxygen octahedral rotations between $PbTiO_3$, LSMO, and $NdGaO_3$, two blocks will display distinct rotation patterns in their LSMO sublayers. It is worth noting that the LSMO bulk exhibits a rhombohedral lattice with a Glazer rotation of $a^-a^-a^-$, whereas $NdGaO_3$ and $PbTiO_3$ possess orthorhombic and tetragonal crystal symmetries with $c^+a^-a^-$ and $a^0a^0a^0$, respectively [27–29]. The interfacial oxygen octahedral coupling can enhance or suppress the degree of oxygen octahedral rotations in LSMO sublayers in proximity to $NdGaO_3$ or $PbTiO_3$. Hence, compared to block A, block B is expected to exhibit the less-rotated oxygen octahedra with the stronger intralayer ferromagnetic coupling of LSMO. Third, the spontaneous polarization in the ferroelectric $PbTiO_3$ layer can modify the charge concentration and distribution in the adjacent LSMO. If assuming an *upward* polarization in the $PbTiO_3$ layer [18,30], block A is expected to have an increased average hole concentration, making it less favored by the ferromagnetic coupling compared to block B that has an optimal charge concentration. Therefore, when considering the intralayer coupling modified by interface engineering regarding oxygen octahedral coupling and charge transfer, the ferromagnetic intralayer coupling will be stronger in LSMO sublayers hosted by block B, resulting in the higher T_C and H_c compared to block A [18,31]. Meanwhile, given that blocks A and B are featured by different intralayer ferromagnetic couplings, the multilayer consisting of two types of LSMO building blocks is anticipated to exhibit two distinct Curie temperatures and coercivities, while the multilayer with only one type of LSMO blocks should have single Curie temperature and coercivity.

B. Characterizations of magnetization switching states in multilayers

The aforementioned model can be easily examined by experimental results. Two multilayer samples have been prepared and their corresponding temperature- and magnetic-field-dependent magnetizations [$M(T)$ and $M(H)$ curves] are plotted in Fig. 2. The first sample is constructed by growing eight periods of ($PbTiO_3$/LSMO) bilayers on the $NdGaO_3$ substrate to build a multilayer with *one* block A and *seven* blocks B (labeled as sample A1B7). In contrast, the second multilayer begins with the deposition of a $PbTiO_3$ sublayer on the $NdGaO_3$ substrate, followed by *eight* periods of ($PbTiO_3$/LSMO) bilayers. Thus, all LSMO sublayers are identically sandwiched by two adjacent $PbTiO_3$ sublayers. This sample, indexed as sample B8, exclusively consists of *eight* blocks B. Hereby, the pair of samples A1B7 and B8 shall display distinct magnetic switching features attributed to the different configurations of LSMO as sketched in Figs. 2(a) and 2(d).

In Figs. 2(b) and 2(c), sample A1B7 clearly exhibits two distinct T_C and H_c. Specifically, two kinks in $M(T)$ are recorded at 267 and 314 K, respectively, corresponding to the two peaks in d^2M/dT^2 in Fig. 2(b). Moreover, two

magnetic coercivities, $H_{c,1}$ and $H_{c,2}$, are observed around -20 and -165 Oe when sweeping the magnetic field from positive to negative. The ratio of the two magnetizations (M_1/M_2) at the intermediate field between $H_{c,1}$ and $H_{c,2}$ is approximately 1:7 in sample A1B7, revealing that *one* block A is softer and therefore more easily reversed than the other *seven* blocks B. This is in line with our interfacial designs discussed above. In the frame of double-exchange-induced ferromagnetic metallic state, as also suggested by Fig. S4 in the Supplemental Material [22], the enhancement (suppression) of oxygen octahedral rotation of LSMO close to the $NdGaO_3$ ($PbTiO_3$) can decrease (increase) the Mn-O-Mn bond angle ϕ. The resultant narrowed (widened) conduction bandwidth w with $w \sim \cos[(\pi-\phi)/2]$ will weaken (strengthen) the ferromagnetic coupling [32–34]. If taking T_C (H_c) to evaluate the thermal (magnetic) stability of spin alignments, the LSMO sublayer with stronger ferromagnetic coupling will require a higher T_C and a larger H_c to disrupt the aligned spins. In addition, $M(H)$ curves obtained at the temperatures below, in between, and above two T_C (i.e., 267 and 314 K) are compared in Fig. S5 in the Supplemental Material [22] to demonstrate the evolution of ferromagnetic phase in sample A1B7. So, the experimental data of sample A1B7 unambiguously supports the concept that the field reversal process of LSMO can be mediated by interface engineering with the modified intralayer ferromagnetic coupling. On the other hand, for sample B8 one would intuitively predict that only one single T_C and H_c should be recorded, because all the LSMO sublayers are sandwiched by two $PbTiO_3$ layers in the same way to have the identical intralayer coupling. Although it is true that only one T_c around 286 K is identified in Fig. 2(e), sample B8 clearly displays two distinct H_c at -155 and -280 Oe, with a M_1/M_2 ratio of 7:3 at intermediate fields as depicted in Fig. 2(f). This ratio obtained from the intermediate switching state indicates that 70% of the total LSMO magnetization (or 5.6 LSMO sublayers out of 8) is parallel to the external magnetic field, while 30% (or 2.4 LSMO sublayers) is antiparallel. Given that the intermediate state observed in sample B8 cannot be easily attributed to the interface engineering discussed earlier, additional magnetic mechanisms need to be considered to fully understand our experimental observations.

The usage of polarized neutron reflectometry (PNR) allows us to identify the layer-resolved magnetization configurations in a magnetic multilayer [35–38]. The reflectivity profiles, which are plotted as a function of the scattering vector Q, are used to probe two distinct magnetization states in samples A1B7 and B8. The first magnetization state (indexed as state I) is defined by the saturated magnetization state, where a large magnetic field of 5000 Oe is applied along [1–10] (indicated as +5000 Oe). The second magnetization state (state II), which resides on the magnetization plateau between $H_{c,1}$ and $H_{c,2}$ to represent the intermediate switching state, is achieved by applying an intermediate magnetic field along [−110] (indicated as -110 Oe for sample A1B7 and -260 Oe for sample B8). It shall be noted that the $M(H)$ loop is difficult to obtain due to the strong paramagnetic background from $NdGaO_3$ at 10 K, so we choose the applied magnetic field for state II based on the $M(H)$ curve measured at 25 K by considering the slight increase of both $H_{c,1}$ and $H_{c,2}$ on cooling (see Fig. S6 in the Supplemental Material [22] for the temperature-dependent $M(H)$ curves of sample B8).

For sample A1B7, the moderate field for state II is chosen as -110 Oe based on the $M(H)$ loop in Fig. 3(a). The corresponding non-spin-flip (NSF) PNR data for states I and II, are compared in Figs. 3(a) and 3(b). At an applied field of 5000 Oe, the saturation magnetization of state I in Fig. 3(a) is characterized by a single, dominant Bragg peak located at $Q = 0.075$ Å^{-1} in both the $R++$ and $R--$ data, corresponding to a real-space periodicity of 83.7 Å ($Q = 2\pi/d$) in agreement with the nominal thickness (81.4 Å) of the LSMO/$PbTiO_3$ bilayer structure. No measurable spin-flip (SF) signal is observed in state I, confirming that the magnetizations of all LSMO sublayers are aligned parallelly to the external field in state I. Sweeping the applied field to -110 Oe from the positive saturation, the reshaped PNR curves are shown for state II in Fig. 3(b). The model, which is the best fit to the PNR data, reveals that the in-plane magnetization across the multilayer comprises of magnetic moments in the top seven LSMO sublayers (blocks B) to align antiparallelly to the applied magnetic field, and the magnetic moment of the bottommost sublayer (block A) parallel to the field for the intermediate state. This configuration is consistent with the $M(H)$ loop of sample A1B7, where the ratio between switched and unswitched magnetization is about 1:7 in the magnetization plateau region between $H_{c,1}$ and $H_{c,2}$. Furthermore, for the best-fit magnetization configurations, the corresponding depth profiles of the nuclear and magnetic scattering length densities for states I and II are plotted in Figs. 3(c) and 3(d), respectively.

On the other hand, the PNR data obtained from sample B8 is summarized in Fig. 4, and the intermediate field is chosen as -260 Oe. Similar to sample A1B7, the NSF profiles of state I for sample B8 can be nicely fit by the homogeneous magnetization parallel to the external field in all eight $PbTiO_3$-sandwiched LSMO sublayers, as plotted in Fig. 4(a). In state II, as depicted in Fig. 4(b), two dominant Bragg peaks, which can be viewed as peak splitting compared to the data obtained from state I, are recorded in the NSF profiles at $Q = 0.077$ Å^{-1} and 0.091 Å^{-1} to suggest a complex magnetization configuration for the intermediate switching state. Furthermore, in order to reproduce the peak splitting in PNR and M_1/M_2 ratio of 7:3 in $M(H)$, the inhomogeneous magnetization within the individual LSMO sublayer must be taken into considerations for state II (also see Figs. S7 and S8 in the Supplemental Material [22]). The best-fit intermediate magnetization configuration can be established by building a gradual change of magnetization crossing the *five* LSMO sublayers that are close to the substrate. The ratio of the magnetization parallel to the external field is gradually increased from 0% to 100% in these five LSMO sublayers from the side of the substrate. Specifically, such parallel magnetization ratios for *eight* individual LSMO sublayers are 0%, 33%, 50%, 67%, 100%, 100%, 100%, and 100% from the substrate side to the sample surface, respectively. Figures 4(c) and 4(d) plot the corresponding nuclear/magnetic scattering length densities for states I and II, respectively. This fitted intermediate magnetization structure gives an estimated magnetization change of 69% (or 5.5 LSMO sublayers), which is close to the experimental data obtained from the intermediate state.

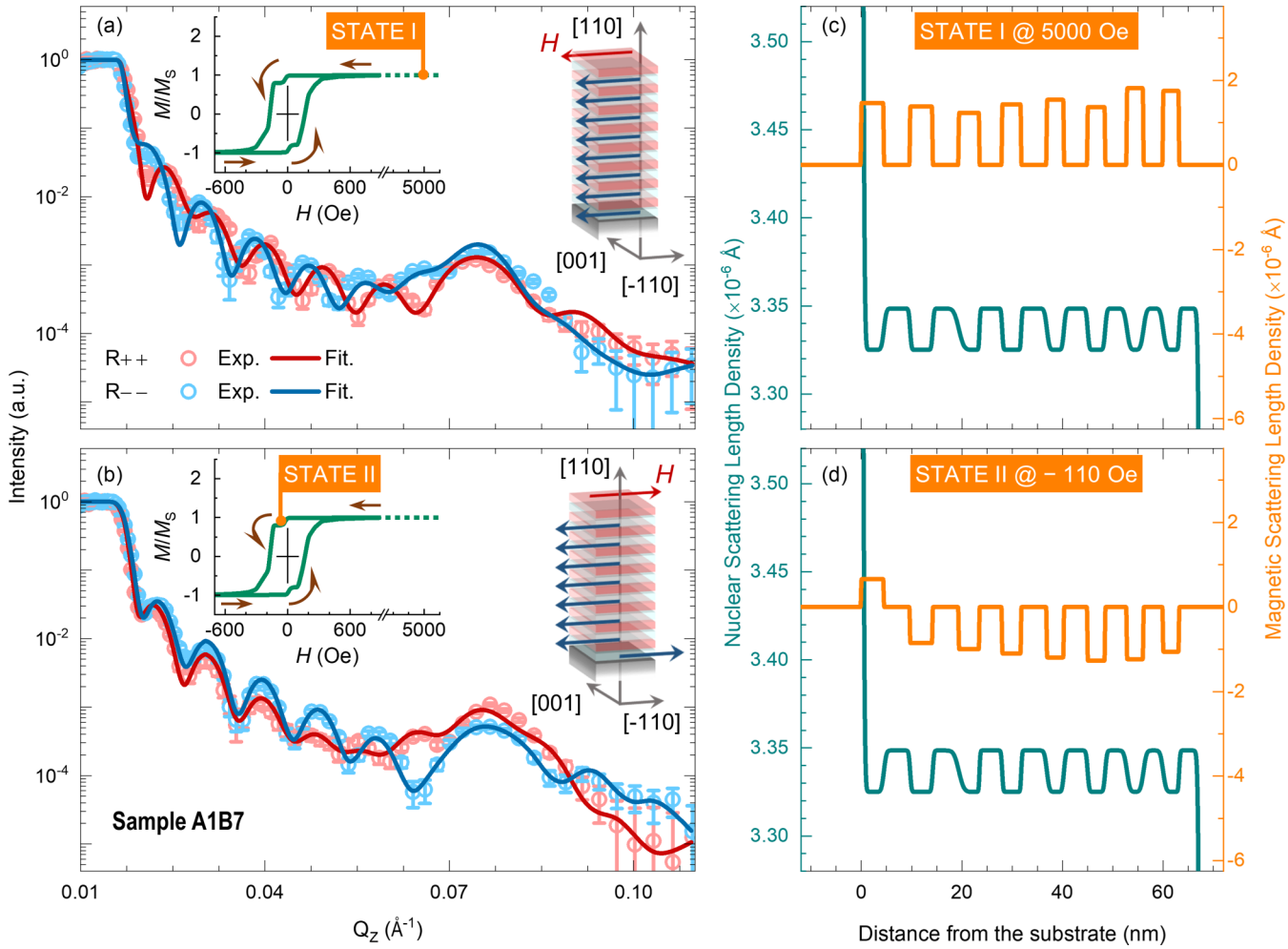

FIG. 3. Layer-resolved magnetization configurations for sample A1B7. The PNR experimental data and fitting curves are plotted for state I (saturated state) in (a) and state II (intermediate state) in (b). Insets: the corresponding $M(H)$ curves and magnetization configurations. A magnetic field of 5000 Oe (indicated as +5000 Oe) is applied along [1-10] to achieve state I, while a field of 110 Oe (indicated as −110 Oe) is applied along [−110] for state II. The depth profiles of the nuclear (green) and magnetic (orange) scattering length densities used for PNR fittings are shown for state I in (c) and state II in (d), respectively.

Given that only one type of LSMO block (block B) is present in sample B8, the observed moment gradient with antiparallel magnetizations cannot be simply accounted for the intralayer coupling that is mediated by the oxygen octahedral rotation and interfacial charge transfer. Other magnetic mechanisms need to be taken into consideration.

C. Possible mechanisms for intermediate switching states

Next, we attempt to interpret the observed intermediate switching states regarding three energy terms, including intralayer coupling E_{intra}, interlayer exchange E_{ex}, and magnetostatic interaction E_{ms}. It is well known that the intralayer ferromagnetic coupling is dominated by the double-exchange interaction, of which the strength is influenced by the doping concentration x and electron hopping bandwidth w along the Mn-O-Mn chain. Typically, for constant x, w decays as a function of the Mn-O-Mn bond length d, i.e., the distance between two magnetic Mn ions, in the power-law form of $w \propto d^{-3.5}$ with d around 4 Å [34,39]. So, the intralayer coupling E_{intra} is strongly mediated by the interface engineering with interfacial charge transfers and octahedral deformations, resulting in distinct magnetic properties such as Curie temperatures from different LSMO blocks. Given that seven blocks B in sample A1B7 as well as eight blocks B in sample B8 give a collective Curie temperature, we believe that the differences of chemical structures and neighbors between blocks B, if any, can be neglected in our samples.

For the second term of interlayer exchange E_{ex}, we consider three possible types of interlayer exchanges, including ferromagnetic, antiferromagnetic, and noncoupling exchanges, across the stack of LSMO/$PbTiO_3$/LSMO in blocks B. If the interlayer exchange is antiferromagnetic, the stacking of blocks B should always exhibit multiple coercivities that are similar to synthetic antiferromagnets [9]. Apparently, this contradicts the experimental data obtained from sample A1B7, where seven blocks B give one collective coercivity in the $M(H)$ curve and PNR data. So, the exchange between LSMO sublayers in blocks B are either ferromagnetic or noncoupling. The nature of interlayer exchange is further elucidated by studying samples A1Bn, where "n" stands for the quantity of blocks B integrated into the multilayer sample.

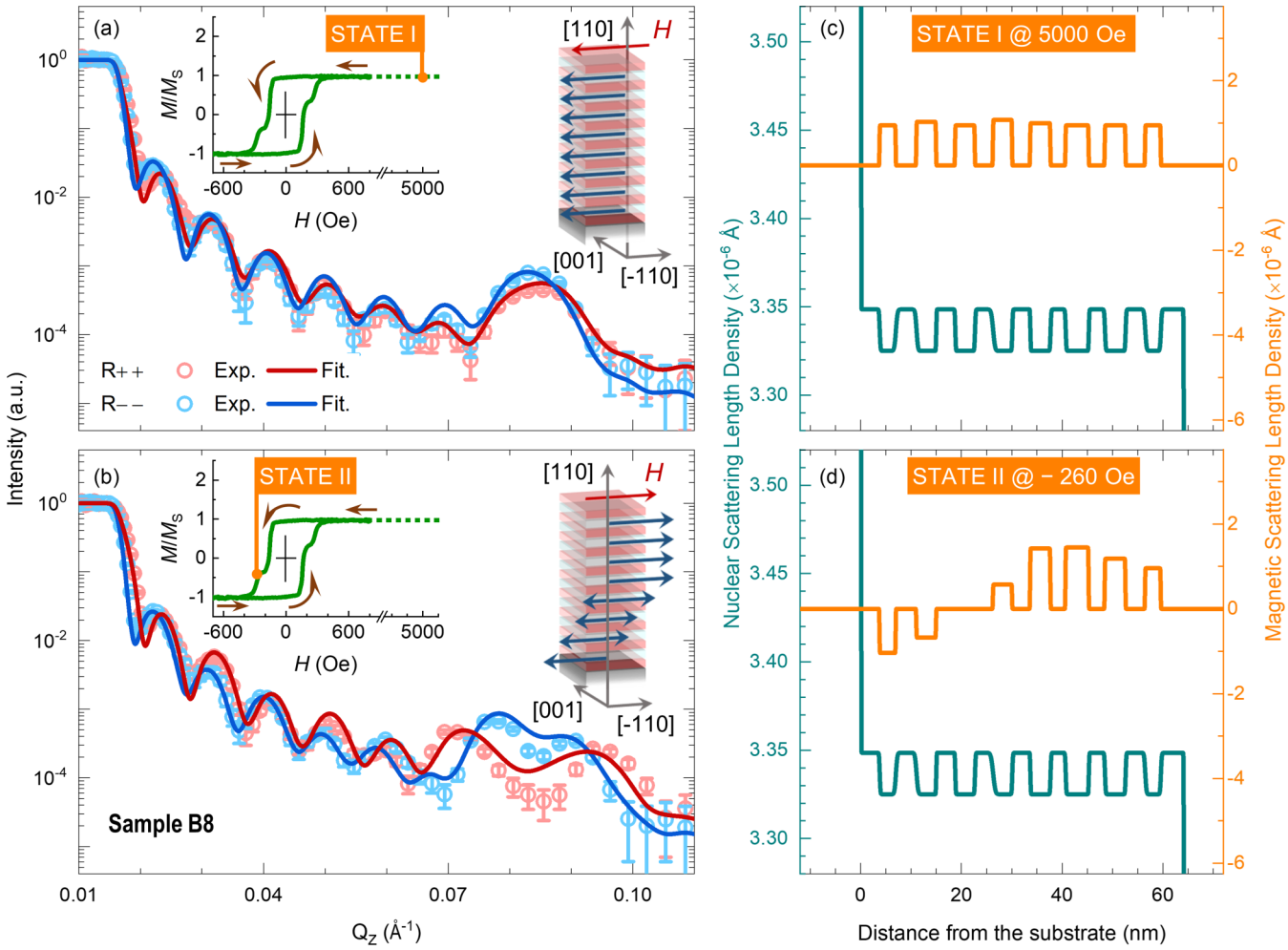

FIG. 4. Layer-resolved magnetization configurations for sample B8. The PNR experimental data and fitting curves are plotted for state I (saturated state) in (a) and state II (intermediate state) in (b). Insets: the corresponding $M(H)$ curves and magnetization configurations. A magnetic field of 5000 Oe (indicated as +5000 Oe) is applied along [1-10] to achieve state I, while a field of 260 Oe (indicated as −260 Oe) is applied along [−110] for state II. The depth profiles of the nuclear (green) and magnetic (orange) scattering length densities used for PNR fittings are shown for state I in (c) and state II in (d), respectively.

It can be inferred that Curie temperature of blocks B must be enhanced (unchanged) with increasing the value of n, if the interlayer exchange is ferromagnetic (noncoupling). As recorded in our previous study [18], the Curie temperature for blocks B was raised monotonously on increasing n, suggesting the ferromagnetic interlayer exchange in blocks B. Therefore, the ferromagnetic interlayer exchange needs to be taken into consideration for the formation of intermediate switching state. Moreover, such ferromagnetic interlayer exchange can be viewed as two spatially separated LSMO sublayers coupled across a 5-nm-thick nonmagnetic $PbTiO_3$ spacer. Usually, the long-distance spin exchanges, such as dipolar interaction [40] or Ruderman-Kittel-Kasuya-Yosida interaction [41], are also featured by a power-law decaying as a function of the distance. In this case, if assuming the power-law exponents of the intralayer coupling and interlayer exchange are close, the interlayer exchange strength E_{ex} would be 3–4 orders of magnitude weaker than the intralayer coupling E_{intra}.

For the third term of magnetostatic energy E_{ms} that prefers a magnetic structure with a minimal net magnetization (or multidomains), the antiparallel magnetization between two neighboring LSMO sublayers will be established. It shall be noted that E_{ms} is usually several orders of magnitude smaller than E_{intra} [42], making E_{intra} a dominant role in determining the intermediate magnetization structure when magnetic sublayers have different E_{intra}. However, if all the magnetic sublayers share the identical E_{intra}, the interplays between E_{ex} and E_{ms} will be highlighted. In the heterostructure of $LSMO/PbTiO_3/LSMO$, the parallel magnetization between two LSMO sublayers is favored by the ferromagnetic E_{ex}, while the antiparallel magnetization is favored by E_{ms}.

Now we focus on the energy status for the intermediate states in both samples. For sample A1B7, two types of interface-engineered LSMO blocks, i.e., blocks A and B, exhibit different values of E_{intra} with two distinct Curie temperatures. Given the overwhelming role of E_{intra}, when an intermediate magnetic field between $H_{c,1}$ and $H_{c,2}$ is applied, the antiparallel magnetization will be formed between $PbTiO_3/LSMO/NdGaO_3$ and $PbTiO_3/LSMO/PbTiO_3$ blocks for the intermediate switching state. On the other hand, sample B8 only contains blocks B with identical E_{intra} for all LSMO sublayers with single Curie temperature. Therefore, the

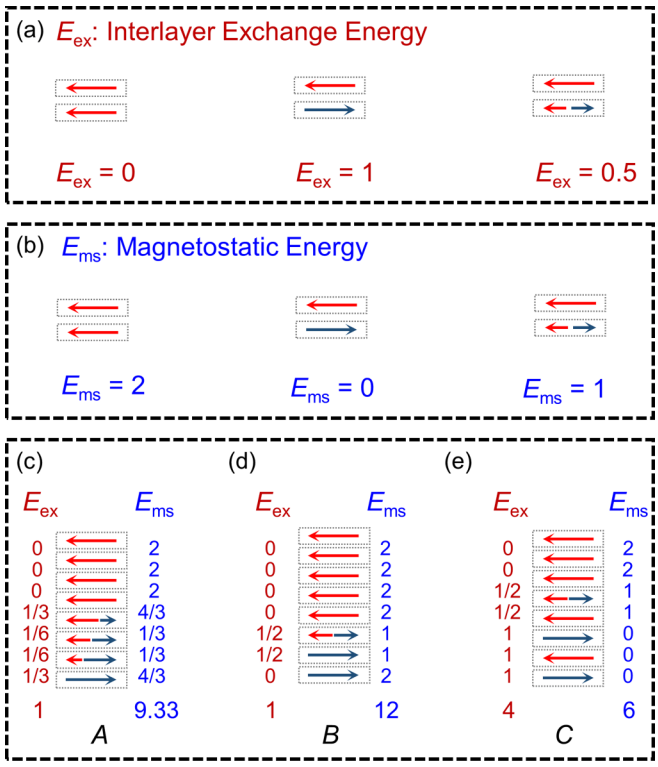

FIG. 5. The definitions of energy scales using bilayer magnetization configurations for E_{ex} in (a) and E_{ms} in (b). (c)–(e) Comparison on E_{ex} and E_{ms} among three typical magnetic configurations where the total magnetization of eight LSMO sublayers are set to mimic the one of sample B8 at the intermediate switching state. The total E_{ex} and E_{ms} are estimated by adding up individual E_{ex} and E_{ms} obtained from seven pairs of LSMO bilayers, respectively.

energy competition between E_{ex} and E_{ms} becomes crucial. As shown in Fig. 5, the semiquantitative analysis is conducted on several typical magnetic structures of LSMO multilayers with the same total intermediate magnetization.

First, the energy scales of E_{ex} and E_{ms} are defined based on the bilayer magnetization in Figs. 5(a) and 5(b) with the neglect of the nonmagnetic spacer. For the ferromagnetic interlayer exchange, the parallel and antiparallel configurations correspond to the low and high E_{ex}, indexed as $E_{ex} = 0$ and $E_{ex} = 1$, respectively. On the other hand, for the magnetostatic interaction that favors the compensated magnetization, the parallel and antiparallel magnetization alignments result in the high and low E_{ms}, labeled as $E_{ms} = 2$ and $E_{ms} = 0$, respectively. Accordingly, for the bilayer that contains one sublayer with 50% parallel/antiparallel mixed magnetization, E_{ex} and E_{ms} will show an intermediate value as $E_{ex} = 0.5$ and $E_{ms} = 1$. Following this method, E_{ex} and E_{ms} can be estimated for different magnetization configurations of LSMO multilayers in Figs. 5(c)–5(e), corresponding to configurations A–C, respectively. If the intermediate state of sample B8 with configuration A, the energy can be labeled as $E_{ex} = 1$ and $E_{ms} = 9.33$, respectively. If increasing the magnetization gradient and constraining the inhomogeneous magnetization within one LSMO sublayer, as shown in configuration B, E_{ex} will be unchanged ($E_{ex} = 1$) with an increased E_{ms} ($E_{ms} = 12$). Hence, configuration A shall be more energetically favored compared to configuration B. Moreover, configuration C in Fig. 5(e) displays the alternative stacking of antiparallelly magnetized sublayers, with a minimized E_{ms} ($E_{ms} = 6$) but a raised E_{ex} ($E_{ex} = 4$). Therefore, the choice between configurations A and C relies on the competition between E_{ms} and E_{ex}. Meanwhile, the fact that the magnetization of LSMO layers close to the $NdGaO_3$ substrate is antiparallel to the external field, as observed in the intermediate state of sample B8, can also be ascribed to E_{ms}. While the paramagnetic nature of $NdGaO_3$ makes the substrate's magnetization parallel to the external field and enhanced on cooling, E_{ms} drives the bottom LSMO layers (close to $NdGaO_3$) to exhibit the antiparallel magnetization to lower the magnetostatic energy. This effect makes the top LSMO layers (away from the $NdGaO_3$ substrate) magnetically softer and leads to the formation of the intermediate switching state in sample B8. Given that the intermediate state inferred from the PNR data adopts a magnetic structure of configuration A instead of C, the reduction of magnetostatic energy cannot fully compensate the rise of interlayer exchange in sample B8. In other words, for the multilayers with an identical intralayer coupling, the interplay between the interlayer exchange and magnetostatic energy plays an important role.

IV. CONCLUSION

In this study, the magnetic switching process in LSMO-based multilayers is investigated. Owing to the application of nonmagnetic $PbTiO_3$ and $NdGaO_3$, two distinct LSMO blocks, i.e., $PbTiO_3$/LSMO/$NdGaO_3$ (block A) and $PbTiO_3$/LSMO/$PbTiO_3$ (block B), are constructed to exhibit different T_C and H_c due to the oxygen octahedral coupling and interfacial charge transfer. Sample A1B7 contains both types of LSMO blocks, thus showing two distinct T_C and H_c. However, sample B8 only consists of one type of LSMO block (block B), but presents two unexpected coercivities. The PNR results uncover the complex magnetic structure, where a gradual change of magnetization is found in the five LSMO sublayers that are close to the substrate, for the intermediate switching state of sample B8. The competition between the interlayer exchange and magnetostatic interaction is discussed to interpret our observations. Our findings contribute to a deeper understanding of the magnetic reversal processes in manganite multilayers and may help develop more efficient and versatile magnetic memory devices for advanced technologies.

ACKNOWLEDGMENTS

This work was supported by the National Natural Science Foundation of China by Grants No. 12104002, No. 12074001, No. 12104008, No. 11974326, No. U2032218, and No. 12204005. G.L.C. acknowledges funding from the Deutsche Forschungsgemeinschaft (DFG, German Research Foundation) under TRR80 (From Electronic Correlations to Functionality, Projects No. 107745057 and No. F7). The authors acknowledge the Australian Nuclear Science and Technology Organisation for the provision of neutron beamtime (under Proposals No. P8425 and No. P9002).

[1] S. Woo, K. Litzius, B. Krüger, M.-Y. Im, L. Caretta, K. Richter, M. Mann, A. Krone, R. M. Reeve, M. Weigand, P. Agrawal, I. Lemesh, M.-A. Mawass, P. Fischer, M. Kläui, and G. S. D. Beach, Observation of room-temperature magnetic skyrmions and their current-driven dynamics in ultrathin metallic ferromagnets, Nat. Mater. **15**, 501 (2016).

[2] W. Jiang, G. Chen, K. Liu, J. Zang, S. G. E. Te Velthuis, and A. Hoffmann, Skyrmions in magnetic multilayers, Phys. Rep. **704**, 1 (2017).

[3] H. Takagi, R. Takagi, S. Minami, T. Nomoto, K. Ohishi, M.-T. Suzuki, Y. Yanagi, M. Hirayama, N. D. Khanh, K. Karube, H. Saito, D. Hashizume, R. Kiyanagi, Y. Tokura, R. Arita, T. Nakajima, and S. Seki, Spontaneous topological Hall effect induced by non-coplanar antiferromagnetic order in intercalated van der Waals materials, Nat. Phys. **19**, 961 (2023).

[4] L. Guo, N. Campbell, Y. Choi, J.-W. Kim, P. J. Ryan, H. X. Huyan, L. Z. Li, T. X. Nan, J.-H. Kang, C. Sundahl, X. Q. Pan, M. S. Rzchowski, and C.-B. Eom, Spontaneous Hall effect enhanced by local Ir moments in epitaxial $Pr_2Ir_2O_7$ thin films, Phys. Rev. B **101**, 104405 (2020).

[5] S. Bhatti, R. Sbiaa, A. Hirohata, H. Ohno, S. Fukami, and S. N. Piramanayagam, Spintronics based random access memory: A review, Mater. Today **20**, 530 (2017).

[6] Y. C. Lau, D. Betto, K. Rode, J. M. D. Coey, and P. Stamenov, Spin-orbit torque switching without an external field using interlayer exchange coupling, Nat. Nanotechnol. **11**, 758 (2016).

[7] F. Trier, P. Noël, J. Kim, J. Attané, L. Vila, and M. Bibes, Oxide spin-orbitronics: Spin-charge interconversion and topological spin textures, Nat. Rev. Mater. **7**, 258 (2022).

[8] C. Song, B. Cui, F. Li, X. J. Zhou, and F. Pan, Recent progress in voltage control of magnetism: Materials, mechanisms, and performance, Prog. Mater. Sci. **87**, 33 (2017).

[9] B. B. Chen, H. R. Xu, C. Ma, S. Mattauch, D. Lan, F. Jin, Z. Guo, S. Y. Wan, P. F. Chen, G. Y. Gao, F. Chen, Y. X. Su, and W. B. Wu, All-oxide-based synthetic antiferromagnets exhibiting layer-resolved magnetization reversal, Science **357**, 191 (2017).

[10] W. M. Lü, S. Saha, X. Renshaw Wang, Z. Q. Liu, K. Gopinadhan, A. Annadi, S. W. Zeng, Z. Huang, B. C. Bao, C. X. Cong, M. Venkatesan, T. Yu, J. M. D. Coey, A. Ariando, and T. Venkatesan, Long-range magnetic coupling across a polar insulating layer, Nat. Commun. **7**, 11015 (2016).

[11] M. Gibert, M. Viret, P. Zubko, N. Jaouen, J.-M. Tonnerre, A. Torres-Pardo, S. Catalano, A. Gloter, O. Stéphan, and J.-M. Triscone, Interlayer coupling through a dimensionality-induced magnetic state, Nat. Commun. **7**, 11227 (2016).

[12] P. F. Chen, Z. Huang, M. S. Li, X. J. Yu, X. H. Wu, C. J. Li, N. N. Bao, S. W. Zeng, P. Yang, L. L. Qu, J. S. Chen, J. Ding, S. J. Pennycook, W. B. Wu, T. V. Venkatesan, A. Ariando, and G. M. Chow, Enhanced magnetic anisotropy and orbital symmetry breaking in manganite heterostructures, Adv. Funct. Mater. **30**, 1909536 (2020).

[13] P. Němec, M. Fiebig, T. Kampfrath, and A. V. Kime, Antiferromagnetic opto-spintronics, Nat. Phys. **14**, 229 (2018).

[14] C. Song, Y. F. You, X. Z. Chen, X. F. Zhou, Y. Y. Wang, and F. Pan, How to manipulate magnetic states of antiferromagnets, Nanotechnology **29**, 112001 (2018).

[15] D. Yi, N. P. Lu, X. G. Chen, S. C. Shen, and P. Yu, Engineering magnetism at functional oxides interfaces: Manganites and beyond, J. Phys.: Condens. Matter **29**, 443004 (2017).

[16] A. Zakharova, M. Caputo, E. B. Guedes, M. Radovic, F. Nolting, and C. Piamonteze, Interplay between magnetism and interface-induced effects in ultrathin manganites, Phys. Rev. Mater. **5**, 124404 (2021).

[17] E. J. Moon, R. Colby, Q. Wang, E. Karapetrova, C. M. Schlepütz, M. R. Fitzsimmons, and S. J. May, Spatial control of functional properties via octahedral modulations in complex oxide superlattices, Nat. Commun. **5**, 5710 (2014).

[18] P. F. Chen, Z. Huang, C. J. Li, B. M. Zhang, N. N. Bao, P. Yang, X. J. Yu, S. W. Zeng, C. H. Tang, X. H. Wu, J. S. Chen, J. Ding, S. J. Pennycook, A. Ariando, T. V. Venkatesan, and G. M. Chow, Binary controls on interfacial magnetism in manganite heterostructures, Adv. Funct. Mater. **28**, 1801766 (2018).

[19] H. Wang, X. Chi, Z. R. Liu, H. Y. Yoong, L. L. Tao, J. X. Xiao, R. Guo, J. X. Wang, Z. L. Dong, P. Yang, C.-J. Sun, C. J. Li, X. B. Yan, J. Wang, G. M. Chow, E. Y. Tsymbal, H. Tian, and J. S. Chen, Atomic-scale control of magnetism at the titanite-manganite interfaces, Nano Lett. **19**, 3057 (2019).

[20] M. James, A. Nelson, S. A. Holt, T. Saerbeck, W. A. Hamilton, and F. Klose, The multipurpose time-of-flight neutron reflectometer "Platypus" at Australia's OPAL reactor, Nucl. Instrum. Methods Phys. Res. A **632**, 112 (2011).

[21] T. Saerbeck, F. Klose, A. L. Brun, J. Füzi, A. Brule, A. Nelson, S. Holt, and M. James, Invited article: Polarization "Down Under": The polarized time-of-flight neutron reflectometer PLATYPUS, Rev. Sci. Instrum. **83**, 081301 (2012).

[22] See Supplemental Material at http://link.aps.org/supplemental/10.1103/PhysRevB.110.054417 for the RHEED, AFM, STEM, *R*(T), *M*(H), SF data and PNR fitting results with samples A1B7 and B8.

[23] Computer program SIMULREFLEC, Laboratoire Léon Brillouin CEA/CNRS, France (2007). Free software and description available at https://sourceforge.net/projects/simulreflec/.

[24] T. F. Zhou, G. Li, X. G. Li, S. W. Jin, and W. B. Wu, Self-generated in-plane superlattice in relaxed epitaxial $La_{0.67}Sr_{0.33}MnO_3$ films, Appl. Phys. Lett. **90**, 042512 (2007).

[25] F. H. Zhang, Z. Huang, G. Y. Gao, P. F. Chen, L. F. Wang, X. L. Tan, and W. B. Wu, Anisotropic-strain-induced antiferromagnetic-insulating state with strong phase instability in epitaxial $(La_{0.8}Pr_{0.2})_{0.67}Ca_{0.33}MnO_3$ films, Appl. Phys. Lett. **96**, 062507 (2010).

[26] S. A. Mabud and A. M. Glazer, Lattice parameters and birefringence in $PbTiO_3$ single crystals, J. Appl. Crystallogr. **12**, 49 (1979).

[27] M. Huijben, G. Koster, Z. L. Liao, and G. Rijnders, Interface-engineered oxygen octahedral coupling in manganite heterostructures, Appl. Phys. Rev. **4**, 041103 (2017).

[28] Z. Liao, M. Huijben, Z. Zhong, N. Gauquelin, S. Macke, R. J. Green, S. Van Aert, J. Verbeeck, G. Van Tendeloo, K. Held, G. A. Sawatzky, G. Koster, and G. Rijnders, Controlled lateral anisotropy in correlated manganite heterostructures by interface-engineered oxygen octahedral coupling, Nat. Mater. **15**, 425 (2016).

[29] H. Sharma, J. Kreisel, and P. Ghosez, First-principles study of $PbTiO_3$ under uniaxial strains and stresses, Phys. Rev. B **90**, 214102 (2014).

[30] S. R. Zhang, Y. L. Zhu, Y. L. Tang, Y. Liu, S. Li, M. J. Han, J. Y. Ma, B. Wu, Z. H. Chen, S. Saremi, and X. L.

Ma, Giant polarization sustainability in ultrathin ferroelectric films stabilized by charge transfer, Adv. Mater. **29**, 1703543 (2017).

[31] Z. L. Liao, N. Gauquelin, R. J. Green, S. Macke, J. Gonnissen, S. Thomas, Z. C. Zhong, L. Li, L. Si, S. V. Aert, P. Hansmann, K. Held, J. Xia, J. Verbeeck, G. V. Tendeloo, G. A. Sawatzky, G. Koster, M. Huijben, and G. Rijnders, Thickness dependent properties in oxide heterostructures driven by structurally induced metal-oxygen hybridization variations, Adv. Funct. Mater. **27**, 1606717 (2017).

[32] D. Lan, P. F. Chen, C. Liu, X. H. Wu, P. Yang, X. J. Yu, J. Ding, J. S. Chen, and G. M. Chow, Interfacial control of domain structure and magnetic anisotropy in $La_{0.67}Sr_{0.33}MnO_3$ manganite heterostructures, Phys. Rev. B **104**, 125423 (2021).

[33] P. F. Chen, D. Lan, C. Liu, X. H. Wu, A. Khandelwal, M. S. Li, C. J. Li, P. Yang, X. J. Yu, J. S. Chen, S. J. Pennycook, A. Ariando, Z. Huang, and G. M. Chow, Correlated cation lattice symmetry and oxygen octahedral rotation in perovskite oxide heterostructures, J. Appl. Phys. **129**, 025303 (2021).

[34] M. Medarde, J. Mesot, P. Lacorre, S. Rosenkranz, P. Fischer, and K. Gobrecht, High-pressure neutron-diffraction study of the metallization process in $PrNiO_3$, Phys. Rev. B **52**, 9248 (1995).

[35] D. Gorkov, B. P. Toperverg, and H. Zabel, Artificial magnetic pattern arrays probed by polarized neutron reflectivity, Nanomaterials **10**, 851 (2020).

[36] G. P. Felcher, Neutron reflectometry as a tool to study magnetism (invited), J. Appl. Phys. **87**, 5431 (2000).

[37] T. L. Meyer, A. Herklotz, V. Lauter, J. W. Freeland, J. Nichols, E.-J. Guo, S. Lee, T. Z. Ward, N. Balke, S. V. Kalinin, M. R. Fitzsimmons, and H. N. Lee, Enhancing interfacial magnetization with a ferroelectric, Phys. Rev. B **94**, 174432 (2016).

[38] D. Schumacher, A. Steffen, J. Voigt, J. Schubert, and T. Brückel, Inducing exchange bias in $La_{0.67}Sr_{0.33}MnO_{3-\delta}/SrTiO_3$ thin films by strain and oxygen deficiency, Phys. Rev. B **88**, 144427 (2013).

[39] P. G. Radaelli, G. Iannone, M. Marezio, H. Y. Hwang, S.-W. Cheong, J. D. Jorgensen, and D. N. Argyriou, Structural effects on the magnetic and transport properties of perovskite $A_{1-x}A'_xMn\,O_3$ ($x = 0.25, 0.30$), Phys. Rev. B **56**, 8265 (1997).

[40] L. C. Sampaio, R. Hyndman, F. S. de Menezes, J. P. Jamet, P. Meyer, J. Gierak, C. Chappert, V. Mathet, and J. Ferré, Power-law relaxation decay in two-dimensional arrays of magnetic dots interacting by long-range dipole-dipole interactions, Phys. Rev. B **64**, 184440 (2001).

[41] B. Zhang, L. Jiang, and Y. Zheng, Long-range and tunable RKKY interaction in the topological channel of gated bilayer graphene, Phys. Rev. B **101**, 155421 (2020); J. Jeon and S. Lee, Anomalous long-distance RKKY interaction in one-dimensional quasiperiodic chains, arXiv:2310.15228.

[42] C. Binns, Tutorial section on nanomagnetism, Front. Nanosci. **6**, 1 (2014).